

# State transition and flaring activity of IGR J17464-3213/H1743-322 with SPI/INTEGRAL telescope

A. Joinet<sup>1</sup>, E. Jourdain<sup>1</sup>, J. Malzac<sup>1</sup>, J.P. Roques<sup>1</sup>, V.Schönfelder<sup>2</sup>, P. Ubertini<sup>3</sup>, F. Capitanio<sup>3</sup>

## ABSTRACT

IGR J17464-3213, already known as the HEAO-1 transient source H1743-322, has been detected during a state transition by the SPI/INTEGRAL telescope. We describe the spectral evolution and flaring activity of IGR J17464-3213/H1743-322 from 2003 March 21 to 2003 April 22. During the first part, the source followed a continuous spectral softening, with the peak of the spectral energy distribution shifting from 100 keV down to  $\sim$  a few keV. However the thermal disk and the hard X-ray components had a similar intensity, indicating that the source was in an intermediate state throughout our observations and evolving toward the soft state. In the second part of our observations, the ASM/RXTE and SPI/INTEGRAL light curve showed a strong flaring activity. Two flare events lasting about 1 day each have been detected with SPI and are probably due to instabilities in the accretion disk associated with the state transition. During these flares, the low (1.5-12 keV) and high (20-200 keV) energy fluxes monitored with ASM/RXTE and SPI/INTEGRAL, are correlated and the spectral shape (above 20 keV) remains unchanged while the luminosity increases by a factor greater than 2.

*Subject headings:* Transient BHC H1743-322

## 1. Introduction

On 2003 March 21, during a scan of the Galactic center region, the new INTEGRAL source IGR J17464-3213 was detected with the IBIS imager (Revnivtsev et al. 2003a). Following this INTEGRAL observation, RXTE observed the same field and found XTE J1746-322

---

<sup>1</sup>CESR, 9 Avenue du Colonel Roche, BP4346, 31028 Toulouse, France

<sup>2</sup>Max-Planck-Institut für Extraterrestrische Physik, Postfach 1603, 85740 Garching, Germany

<sup>3</sup>IASF-CNR, via del Fosso del Cavaliere 100, 00133 Roma, Italy

at a position consistent with that of IGR J17464-3213 (Markwardt & Swank 2003) with a hard spectrum (with a powerlaw photon index  $\Gamma$  of  $\simeq 1.49 \pm 0.01$ ), while a radio counterpart has been identified with the VLA (Rupen et al. 2003a). All the positions were compatible (Remillard 2003) with the H1743-322 transient source discovered during its outburst in 1977 by Ariel V and HEAO-1 (Kaluzienski & Holt 1977a) which had a maximum observed flux of 730 mCrab (Kaluzienski & Holt 1977b).

Early 2003, INTEGRAL observations showed a slowly rising hard X-ray flux. That was the beginning of a long outburst which lasted until the end of November 2003. During this period, the source was monitored by RXTE (Homan et al. 2004; Remillard et al. 2004) and Chandra (Miller et al. 2004) showing the occurrence of various spectral/timing states. In some of them it showed high frequency quasi-periodic oscillations at 240 Hz and 160 Hz (therefore in the 3:2 ratio which has recently emerged in a few Galactic black hole systems) compatible with the dynamical time-scale at the innermost stable orbit around a 10 solar mass black hole. The presence of dips in the X-ray light curves suggests a large inclination ( $\sim 60\text{-}70^\circ$ ) (Homan et al. 2004). Observations with the VLA showed intense radio activity, in particular a strong radio flare was reported on April 8 associated with a jet (Rupen et al. 2003b). Infrared (Baba et al. 2003) and optical (Steeeghs et al. 2003) counterparts were reported and found to be consistent with emission from a jet. The ASM/RXTE light curve of the 2003 outburst is presented in Fig. 1. Its profile is more complex than the fast rise slow decay of classical X-ray novae, but shows some similarities with other transient black hole X-ray binaries in outburst such as XTE J1859+226 (Brocksopp et al. 2002), GRO J1655-40 (Remillard et al. 1999) or XTE J1550-564 (Sobczak et al. 2000).

Due to the source location near the Galactic Center, further INTEGRAL observations of IGR J17464-3213 were carried out in the framework of the Galactic Centre Deep Exposure (GCDE) of the core program (Winkler et al. 2003) in March, April, August and September 2003 (Parmar et al. 2003; Lutovinov et al. 2004; Capitanio et al. 2005). While these monitoring campaigns may suggest a smooth evolution from the hard to the soft state, RXTE observations, together with a bigger set of data, allow us to study more in detail the single phases of the source evolution during the rising part of the outburst. The timing results, which can be seen from Table 1 in the H17433-322 paper by Remillard et al. (2004) together with the overall X-ray colour evolution, suggest, referring to the McClintock & Remillard (2003) classification, the following spectral state evolution : "off"  $\rightarrow$  hard  $\rightarrow$  intermediate  $\rightarrow$  SPL  $\rightarrow$  thermal dominant  $\rightarrow$  SPL  $\rightarrow$  intermediate  $\rightarrow$  SPL  $\rightarrow$  thermal dominant  $\rightarrow$  hard  $\rightarrow$  "off" (shown on Fig. 1).

To summarize, the timing and spectral properties of the source indicate a low mass X-ray

binary harboring a black hole observed at large inclination (Homan et al. 2004; Lutovinov et al. 2004).

We present here the results of the SPI instrument observations on board INTEGRAL together with PCA/RXTE data for the X-ray emissions, during Spring 2003, at the beginning of the outburst when the source was evolving through an intermediate state.

Some IBIS and JEM-X data obtained during the same observations have already been published in Parmar et al. (2003) and Capitanio et al. (2005). Here we use a much larger set of SPI data (all the publicly available data) to study in more detail the spectral evolution of H1743-322.

## 2. SPI/INTEGRAL instrument

SPI (Spectrometer for Integral, Vedrenne et al. 2003) is one of INTEGRAL’s two main instruments. Working in the 20 keV - 8 MeV energy domain with 19 hexagonal germanium detectors, it possesses an excellent energy resolution on a 16 degree (corner to corner) field of view.

Careful calibration performed before launch using radioactive sources (Atti et al. 2003) and extensive modelling of the instrument led to a precise determination of its response. The imaging and spectral performance has since been verified in flight (Roques et al. 2003). The knowledge of the SPI instrument along with its spectroscopic capabilities allows us to obtain precise results for the spectral behaviour of X/ $\gamma$ - ray sources.

SPI’s imaging capability is limited but it reaches a  $2.5^\circ$  angular resolution thanks to a HURA (Hexagonal Uniform Redundant Array) coded mask, whose cells have the same size as the individual detectors. Due to the small number of detectors (pixels), SPI image reconstruction methods are based on a combination of data from several pointings separated by 2 degrees and covering the same sky region (“dithering strategy”, see Jensen et al. 2003).

During the  $\simeq 3$  day INTEGRAL revolution, the observing schedule consists of fixed pointings lasting approximatively 30-40 minutes, with a complete dithering pattern made up of 7 (in hexagonal mode) or 25 pointings (in rectangular mode) separated by a  $2^\circ$  angular distance. The latter one is the most commonly used mode. This method increases the amount of data in excess of the number of unknowns and allow to better determine the background and the position and the flux of sources on the detector plane.

### 3. Data

The analysis presented here is based on the data recorded from revolution 53 starting 2003 March 21 to revolution 63 finishing 2003 April 22 (it corresponds to MJD 52719-52751). Some pointings had to be removed due to several reasons. For strong sources, if the projected area onto the detection plane and/or the number of pointings are insufficient, it leads to a lack of sensitivity and/or number of equations to solve (1). Consequently the source flux is determined with huge error bars. Sco X-1 and in certain cases 4U 1700-377 appear in a too small part of a dithering pattern, leading to artefacts during the image reconstruction process. We excluded such pointings and also those affected by a solar flare or by exit/entry into the radiation belts. Otherwise, the background is generally stable. Table 1 gives the details of each revolution. The 230 pointings used for the SPI data analysis give a useful exposure time of  $\sim 333$  ks.

Public PCA/RXTE data, covering some part of the SPI/INTEGRAL data observation periods, were available. Table 1 summarizes the set of PCA/RXTE observations performed under the program ID 80138 and 80146.

### 4. Analysis method

#### 4.1. SPI data analysis

The signal recorded by the SPI camera on the 19 Ge detectors is composed of the contribution from each source in the field of view through the instrument aperture plus the background, which comes mainly from the interaction of high energy particle ( coming from cosmic ray or due to solar activity) with the instrument.

For  $N_s$  sources present in the field of view, the data  $D_p$  obtained during a pointing  $p$  for a given energy band, can be expressed by the relation:

$$D_p = \sum_{i=1}^{N_s} R_{p,i} \times S_{p,i} + B_p \quad (1)$$

where  $R_{p,i}$  is the response of the instrument for the source  $i$ ,  $S_{p,i}$  the flux of the source  $i$  and  $B_p$  the background recorded during the pointing  $p$ .  $D_p$ ,  $R_{p,i}$  and  $B_p$  are vectors of 19 elements.

It is mandatory to reduce the number of unknowns related to the background. In the present work, we describe the background as  $B_p = A_p U$  where  $A_p$  is the normalization coefficient per pointing and  $U$  the "uniformity map" of the SPI camera. This uniformity map is derived

from an empty field observation.  $N_d \times N_p$  The system consists of  $N_d$  (number of detectors)  $\times N_p$  (number of pointings) equations solved simultaneously by a chi-squared minimisation method. The number of unknowns (free parameters) is  $N_p \times (N_s + 1)$  (for the  $N_s$  sources and the background fluxes) but we can limit them by assuming that the time variability for the sources and the background is longer than a single pointing.

The timescales are chosen depending on the goal of the analysis. For the image reconstruction, performed by the SPIROS detection algorithm (Skinner & Connell 2004), source and background fluxes are assumed to be constant during the whole set of observations. Using an iterative source research technique, implemented for the coded mask telescope SPI/INTEGRAL, the source positions are extracted. The fluxes determined in this way are thus rough mean fluxes, the main goal being to extract source positions.

When wishing to build the light curves of the sources detected in the field of view, we must choose the appropriate time scales for each component (source and background).

Concerning the background flux, the global count-rates registered with the Anti-Coincidence System (ACS) indicate that the background flux evolves within a single revolution. A timescale of 6 hours seemed to be the best value to describe the background variability during our observations. For the point-like sources, it is important not to oversample the temporal variability as this increases the error bars and gives no further scientific information. We have chosen a time scale for each source mainly as a function of its intensity and of its temporal behavior. The fainter sources have been considered to have a constant flux within a revolution. For the brightest sources, we test several values and choose the longest timescale over which the source is found not to vary (see below).

Spline functions are used in order to divide one interval of observations (one revolution or part of it) into several subintervals ( $\Delta t_i \geq$  pointing duration) during which the flux of the  $i$ -th component (source or background) is constant.

The system of  $N_p \times N_d$  equations (1) is thus completed by a number of additional constraints reflecting the non-variability of a given parameter ( $S_{i,p}$  or  $A_p$ ) over its timescale ( $\Delta t_i$ ). Its resolution by the chi-squared minimisation method gives the light curves of all components simultaneously.

The count spectra are constructed by solving a similar system in a number of energy bands and then deconvolved using the energy response matrix corresponding to each pointing (Sturmer et al. 2003) to get the photon spectra.

## 4.2. RXTE Spectral reduction

We analysed the PCA/RXTE (Proportional Counter Array) (Bradt et al. 1993) data. The data reduction in the 3-20 keV energy range were performed using the "ftools" routines in the HEASoft software package distributed by NASA's HEASARC. The spectrum extraction was performed from data taken in "Standard 2" mode. The response matrix and the background model were created using ftools programs. Background spectra were made using the latest "bright source" background model. We used all available PCUs for the first part of observations. Since PCU#2 was the detector always in use during the observations from rev. 60 up to 63, it has been used for the data extraction in order to sum several spectra. We added 0.8% up to 7 keV and 0.4% above 7 keV as systematic error.

## 5. Results

### 5.1. Images

The SPI images were built with the SPIROS detection algorithm (Skinner & Connell 2004). We used a catalogue of known sources with their theoretical positions and searched for 15 sources in this catalogue plus 5 possible new sources. The image of the sky observed by SPI in the 20-36 keV energy range in the crowded region of the Galactic Centre can be seen in Figure 2, for where H1743-322 is in the field of view. H1743-322 is the strongest source (247 mCrab) with a significance of  $127 \sigma$  during the total exposure time. H1743-322 is relatively isolated since there are no detected sources within a distance of 2.5 degrees. Table 2 summarizes the 13 sources surrounding H1743-322 in the 20-36 keV energy range. Beyond 90 keV, there are only 3 sources having a significance greater than  $5 \sigma$  and H1743-322 is the most significant one.

### 5.2. Light curves

The light curve of H1743-322 (Figure 3) in the 20-36 keV energy range was constructed using the method described in Section 3, taking into account the 14 sources identified in the field of view (Table 2). We have kept the flux of fainter sources constant and fixed timescales for the 3 more intense on the basis of their variability and of their flux intensity: of 7200 seconds for H1743-322, 86400 seconds for 1E 1740.7-2942 and 10800 seconds for 4U 1700-377 which is known to be variable. The SPI light curve is similar to that published in Capitanio et al. (2005) from IBIS data, except for the bursts around MJD 52743 and 52749 for which

we added new released data to complete our analysis. In order to extend the spectral coverage towards lower energy, we extracted the light curve obtained by ASM/RXTE in the 2-12 keV domain in the same period of observation (data taken from the public XTE database: <http://xte.mit.edu/lcextrct/asmsel.html>).

Since the beginning of the RXTE measurements in 1996, until the beginning of our observations (i.e. 7 years) the source was remaining in an "off" state. Then its intensity increases rapidly over a month culminating in a huge outburst which spans several months with a maximum at MJD 52753.

We see a clear variability of the source on various timescales with initially an enormous flux increase over 3 days. From the "off" state (with an upper limit at  $2\sigma$  of 20 mCrab at MJD 52719), the 20-36 keV flux increases by a factor of 3.7 between MJD 52724-52727 ( $89 \pm 13$  mCrab) and MJD 52729 ( $328 \pm 11$  mCrab). Meanwhile, the ASM flux increases up to  $\sim 200$  mCrab by the same factor.

Then, while the SPI fluxes decrease from MJD 52729 to MJD 52742, the ASM flux follows an opposite behavior. Note that a radio flare occurs around revolution 58 (MJD 52736) with a radio flux increase of a factor 5 between April 6th and 8th (Rupen et al. 2003b) (see Figure 3).

In a second phase, the both emissions are dominated by flaring activity with  $\sim 1$  day bursts (MJD 52744.6 in revolution 61 and MJD 52749.7 in revolution 63) during which the flux is typically multiplied by 2 or 3. Although the long timescale trends are opposite, the soft X-ray and hard X-ray emission are perfectly correlated inside these flares.

We can thus conclude that two distinct time scale modes contribute to the observed light curves: one on a weeks timescale, which we will relate to a state transition (see below), the other mode is on a day timescale and produces simultaneously soft and hard X-rays. This behavior is reminiscent of Cygnus X-1 one, recent observation showing a basically constant spectral shape on short time scale ( $\simeq$  hours) flux variability (Bazzano et al. 2003).

### 5.3. Hardness evolution

In order to study the spectral evolution of the source, we have examined the hardness ratios in the 20-90 keV energy range, defined as  $H = \frac{Counts(36-90keV)}{Counts(20-36keV)}$ . All the fluxes are expressed in mCrab to allow comparison with other instruments.

Figure 4 shows the evolution of the hardness for revolutions 54 to 63. We clearly see 2 groups of points, with mean fluxes of  $\sim 220$  and  $\sim 460$  mCrab respectively. During the

low level flux periods, there is a clear hardness-flux anti-correlation with a linear correlation factor of  $\simeq -0.7$ . It shows clearly the transition from the hard state to a softer state on a timescale of  $\sim 2$  weeks. Conversely, the flux increases at constant hardness during the flare events of revolutions 61 and 63. We also note that data from revolution 56 are not in the continuity of the revolutions 54-55 and 57. But they could correspond to a flux increase with a constant hardness (see the horizontal arrow in Fig. 4) relatively to the anticorrelation trend.

#### 5.4. Spectral modelling

Following the temporal evolution described above, we have compared the spectra corresponding to revolutions 54-55, 56 and 58 in Fig. 5. For each of them, we have put together the deconvolved SPI and PCA/RXTE spectra. The spectral evolution is characterized by the peak of the maximum of the energy moving progressively from 80 keV to a few keV, illustrating the hard to the intermediate state transition.

To study the intermediate and SPL state (revolutions 58 to 63), we separate flare and non flare emissions, the flare state being defined by a 20-36 keV flux greater than 350 mCrab (see Figure 3). Figure 6 shows an increase in the X-ray emission alone between revolutions 58 and 60-63, flares excluded, while the flare spectrum is shifted by a factor of 2 above the non-flare spectrum, keeping roughly the same shape from 5 to 200 keV.

To better quantify the spectral evolution, we have first fitted PCA and SPI data separately.

We used the standard XSPEC 11.3.1 fitting package to fit the PCA data in a 3-20 keV range. These data were modelled with several components. In all cases, the spectral continuum is described by a multicolor disk black body (DISKBB in XSPEC) (Mitsuda et al. 1984) plus a powerlaw. We account for interstellar absorption using PHABS in XSPEC. Individual fits revealed that  $N_H$  was consistent with  $2.3 \times 10^{22} \text{ cm}^{-2}$  as determined by Miller et al. (2004). The  $\chi^2$  was acceptable after including an iron emission line modelled by a narrow Gaussian centered and fixed at 6.4 keV. A smeared iron edge (Ebisawa et al. 1994) (SMEDGE in XSPEC) -which is kept free- of 6-7 keV improves the  $\chi^2$ . The smearing width has been always fixed to 10 keV. The result of spectral fits in the 3-14 keV band with this model is reported in Table 3. The photon indices increase from 1.4 (rev. 55) up to 2.6 (rev. 60-63) in the PCA/RXTE band while the index in the 20-300 energy range, obtained by fitting SPI data by a single powerlaw, increases from 1.8 to 3.1. This spectral evolution is clearly related to the transition from the hard to a softer state. These values are comparable

with the values obtained by HEAO-1 during the 1977-1978 outburst, with the 13-80 keV flux varying from 140 to 100 mCrab and the powerlaw index from 2.6 to 2.2 ( $\pm 0.2$ ) (Cooke et al. 1984; Levine et al. 1984).

Secondly, we fit the 2 instruments together. A basic cross-calibration of the instruments has been performed by comparing the Crab spectrum of both instruments at 30 keV. A normalization factor of 0.96 for the PCA data relative to the SPI data has been determined. However, as the RXTE observations were never performed during the corresponding SPI observation periods (see Table 1), this factor has been kept free. Particularly, during the flaring period of revolution 63, RXTE observations missed the lowest flux part registered during the SPI observations. This explained the low normalization factor obtained for the average spectrum of the flare state.

The PCA and SPI spectra have been fitted together using several models. In all cases, the RXTE spectra have been fitted using the model presented above, the powerlaw component was replaced first by a powerlaw plus cutoff model (CUTOFFPL in XSPEC), then by COMPTT and PEXRAV model to adjust the high energy emission. First, we found, using *ftest* (in XSPEC), that an exponential cutoff is required for all revolutions. However, from revolution 60, the energy cutoff is poorly constrained (see table 4). Moreover the powerlaw slope was found to be equal to the one determined when the RXTE data was fitted separately ( $\Gamma_x = \Gamma'_\gamma$ ).

With the Comptonization model COMPTT (in XPSEC), the temperature of the disk ( $T_{in}$ ) in the multicolor disk blackbody model is forced to be equal to the soft photon temperature ( $T_o$ ) of the Comptonization model. We see in Table 5 that the optical depth decreases from about 3.0 down to 0.3 while the temperature increases from 15 up to  $\simeq 40$  keV. We notice that the best fit parameters obtained for the data set of revolutions 60 to 63 with and without flaring activity are very close.

Then, we used a reflection model (PEXRAV in XSPEC), which is justified by the presence of an iron line in all the spectra. The fit parameters are described in Table 6. During the transition hard to intermediate state, the energy cutoff increases with the powerlaw photon index increases, while a reflection scaling factor of about 0.5 has been found (or fixed) but is poorly constrained

## 6. Discussion

The spectral evolution of the source during the rise to the peak of the outburst can be described in two phases:

- (1) During the first two weeks, the spectrum undergoes a gradual softening associated with the peak of the SED (spectral energy density) shifting from 80 keV in the hard state down to 10 keV on April 8 (rev. 58) (Figure 5) and leading to a clear Hardness-Flux anti-correlation (Figure 4).
- (2) Once this softer state is reached the source shows no significant spectral evolution despite substantial changes in luminosity. The source exhibits flaring activity on a time scale of 1 day during which, the spectral shape remains unchanged from soft to hard X-rays while the flux intensity changes by a factor 2-3.

This spectral evolution is illustrated in figure 7 which displays the evolution of the source in the bolometric luminosity versus hardness plane. During phase 1 the hardness decreases with little changes in luminosity, while during the second phase (after revolution 58) the source exhibit large variations in luminosity at nearly constant hardness.

In Chandra and RXTE observations taken in May 2003 (Miller et al. 2004), the black-body component dominates the spectral emission. The same behaviour is observed in August 2003 in JEM-X data with a non-detection by IBIS (Capitanio et al. 2005). On the other hand, during our observing period the contribution of the thermal disk component to the 2-20 keV flux remained below 32 % (see table 4), and well below the 75 % criterion defining the thermal dominant state (McClintock & Remillard 2003). Therefore the source remained in an intermediate State (IS) or in a Steep Power Law state (SPL) (according to the classification of McClintock & Remillard (2003)) at least until April 22 (MJD 52751) .

In the hard state, the hard X-ray emission is generally believed to be dominated by a hot geometrically thick optically thin accretion flow (Shapiro et al. 1976; Narayan & Yi 1994) surrounded by a cold geometrically thin disk (Shakura & Sunyaev 1973)<sup>1</sup>. Phase (1) of the outburst could be due to the gradual decrease of the inner radius of the cold accretion disk, associated with either the cold disk penetrating the hot inner flow, or the latter collapsing into an optically thick accretion disk with small active regions of hot plasma on top of it (Zdziarski et al. 2002). In both cases the enhanced soft photon flux from the disk tends to cool down the hot phase, leading to softer spectra. Our observations tend support this picture: our fits indicate that as the hard X-ray spectrum softens, both the inner disk temperature and flux grow progressively, as expected when the accretion disk surface and emission increase (see Tables 5). Although the best fit parameters obtained with the Comptonization model show an increase of the hot plasma temperature, the Compton parameter  $y = 4\tau kT/m_e c^2$

---

<sup>1</sup>See Markoff et al. (2001) and Markoff & Nowak (2004) for alternative models for the hard state involving a significant fraction of the hard X-ray emission due to the jet

decreases by a factor of 5. As the  $y$  parameter is related to the ratio of Compton luminosity  $l_h$  (heating of the hot plasma) to the soft seed photons luminosity  $l_s$  ( $y \simeq l_h/l_s$ ), this evolution is consistent with an increase of soft photon flux relative to the heating power. This enhanced cooling can be seen more directly from luminosity measurements, by estimating the ratio  $l_h/l_s$  as  $\Phi_{\text{bol}}/\Phi_{\text{bb}}$  ( $\Phi_{\text{bol}}$  is the bolometric luminosity in the 2-200 keV energy range shown in figure 7), which, from the numbers shown in Table 5 and in figure 7 decreases by a factor of about 5, i.e. roughly consistent with the evolution independently deduced from the Comptonization model. The observed increase of the hot plasma temperature despite an enhanced soft cooling, is due to the fact that the optical depth decreased by a larger amount reducing the efficiency of the energy transfer from electrons to photons.

The diminishing optical depth could have several causes: for instance, the presence of a strong hot comptonizing corona is known to be closely associated with the steady compact jet of the hard state (Corbel 2004; Fender et al. 2004, hereafter FBG04) and it has been suggested that the hot corona forms the base of the jet. The decrease of the coronal optical depth as the source evolves toward the soft state could be related to the disappearance of the compact jet. The fact that the transition from phase (1) to phase (2) appears coincident with a major radio outburst, most likely associated with an ejection event (Rupen et al. 2003b), suggests that most of the coronal material could have been wiped out or ejected during this and possibly other less prominent ejections. Alternatively, it is possible that, as the hot plasma condensates into an optically thick disk, the remaining material in the hot corona has a lower density.

During phase (2), the overall geometry would be globally stable despite instabilities leading to chaotic light curves with little spectral variability. Such a strong variability could be due to local disk instabilities or strong flares in the corona associated with magnetic reconnection events as those inferred in the soft states of Cygnus X-1 (see Zdziarski et al. 2002). Radio emissions lead naturally to assume the presence of a jet, at least temporarily. Alternative models including jets should thus be considered as they can contribute to hard X-ray emission as already proposed by different teams (e.g. Petrucci et al. 2004, Markoff et al. 2001, Georganopoulos et al. 2002).

The presence of a strong radio flare during the state transition seems to be common among black hole transients (Corbel 2004; FBG04). FBG04 provides an interesting interpretation: during the initial softening, the mildly relativistic jet associated with the canonical low/hard state persists, but as the disk makes its inward collapse, the jet becomes unstable and the Lorentz factor rapidly increases, resulting in an internal shock in the outflow, which is the cause of the strong optically thin radio emission.

As we compare the behaviour of H1743-322 with that of other transients, it is worth noting that, even though appearing during the softening period, near the transition from the intermediate to the SPL state, the radio emission occurs during the rising part of the outburst and precedes the soft/hard X-ray peak emission. From this point, H1743-322 is clearly atypical. From Table 3 in Brocksopp et al. (2002), we see that the radio emission occurs after and sometimes (2 cases) simultaneously with the X-ray maximum emission. The flaring activity following the radio emission could be related to the unstable state of the jet as proposed by FBG04.

## 7. Conclusions

The (re)discovery by INTEGRAL of IGR J17464-3213/H1743-322 led to the collection of an important amount of data on this source. H1743-322 shows a rather typical behaviour of black hole candidates with the presence of various spectral states. We analysed the SPI/INTEGRAL and PCA/RXTE observations recorded in March and April 2003, which cover the rising part of the outburst up to the beginning of the maximum of the X-ray emission. Initially in a standard hard state, the source spectrum gradually softened until around April 8 when a major radio flare was reported. In the framework of the comptonization model, this softening phase can be associated with an optical depth decrease (from  $\sim 3$  down to  $\sim 0.3$ ). After the radio flare, the hard X-ray spectral shape seemed to remain unaffected by a strong (X and  $\gamma$ -ray) flaring activity. We tentatively identified the softening phase as the intermediate state and the flaring phase as the SPL, and we note that during the outburst of H1743-322 X-ray transient, the end of the softening phase and the optically thin radio outburst are not associated with the peak of the soft/hard X-ray luminosity.

The SPI project has been completed under the responsibility and leadership of the CNES. We are grateful to ASI, CEA, DLR, ESA, INTA, NASA and OSTC for support. Specific softwares used for this work have been developed by L. Bouchet. A.J. acknowledges Emrah Kalemci for its advices concerning RXTE data analyses. We are grateful to referee for its very fruitful comments, which have clearly improved the paper.

## REFERENCES

- Atti, D., Cordier, B., Gros, M., et al., 2003, *A&A*, 411, L71
- Baba, M.A. , Nagata, T., Iwata, I., Kato, T., & Yamakoa, H., 2003, *IAU Circ.*, 8112

- Bradt, H.V., Rothschild, R.E., & Swank, J.K., 1993, *A&AS*, 97, 355
- Bazzano, A., Bird, A. J., Capitanio, F., et al., 2003, *A&A*, 411, L389
- Brocksopp, C., Fender, R. P., McCollough, M., et al., 2002, *MNRAS*, 331, 765
- Capitanio, F., Ubertini, P., Bazzano, A., et al., 2005, *ApJ*, 622, 503
- Cooke B.A., Levine A.M., Lang F.L., Primini, F.A., & Lewin, W.H.G., 1984, *ApJ*, 285, 258
- Jensen, P. L., Clausen, K., Cassi, C., Ravera, F., Janin, G., Winkler, C., & Much, R., 2003 *A&A*, 411, L7
- Corbel, S., 2004, Review for "X-ray Timing 2003: Rossi and Beyond", edited by P. Kaaret, F.K. Lamb, and J.H. Swank, 2004 AIP, astro-ph/0409155
- Ebisawa, K., Ogawa, M., Aoki, T., Dotani, T., Takizawa, M., Tanaka, Y., Yoshida, K., Miyamoto, S., Iga, S., Hayashida, K., Kitamoto, S., Terada, K., 1994, *PASJ*, 46, 375
- Fender, R. P., Belloni, T.M., & Gallo, E., 2004, *MNRAS*, 355, 1105
- Georganopoulos, M., Aharonian, F. A., Kirk, J. G, 2002, *A&A*, 388, L25
- Homan, J., Miller, J.M., Rudy, W., van der Klis, M., Belloni, T., Steeghs, D., Lewin, W.H.G., 2004, *A&A*, in press, astro-ph/0406334
- Kaluziński L.J. & Holt S.S., 1977a, *IAU Circ.*, 3099
- Kaluziński L.J. & Holt S.S., 1977b, *IAU Circ.*, 3104
- Kong, A. K. H., Kuulkers, E., Charles, P.A., & Homer, L., 2000, *MNRAS*, 312, L49
- Levine, A. M., Lang, F. L., Lewin, W. H. G., et al., 1984, *ApJS*, 54, 581
- Lutovinov, A., Revnivtsev, M., Molkov, S., & Sunyaev, R., 2004, *A&A*, 430, 997
- Markoff, S., & Nowak, M. A., 2004, *ApJ*, 609, 972
- Markoff, S., Falcke, H., & Fender, R., 2001, *A&A*, 372, L25
- Markwardt, C.B., & Swank, J.H., 2003, *Atel* 133
- McClintock, J.E., & Remillard, R.A., 2003, in "Compact in "Compact Stellar X-ray Sources," eds. W.H.G. Lewin and M. van der Klis, Cambridge University Press., astro-ph/0306213

- Miller, J.M., Raymond, J., Homan, J., et al., 2004, ApJ, in press, astro-ph/0406272
- Mitsuda, K., Inoue, H., Koyama, K., et al., 1984, PASJ, 36, 741
- Narayan, R. , & Yi, I., 1994, ApJ, 428, L13
- Parmar, A. N., Kuulkers, E., Oosterbroek, T., Barr, P., Much, R., Orr, A., Williams, O. R., & Winkler, C., 2003, A&A, 411, L421
- Petrucci, P. O., Ferreira, J., Tricot, S., Pelletier, G., Cabanac, C., Henri, G., Chinese J. Astron. Astrophys., in press, astro-ph/0409194
- Poutanen, J., & Svensson, R., 1996, ApJ, 470, 249
- Remillard, R. A., Morgan, E. H., McClintock, J. E., Bailyn, C. D., & Orosz, J. A., 1999, ApJ, 522, 397
- Remillard, R. A., 2003, Atel 138
- Remillard, R.A., McClintock, E.J., Orosz, J.A., & Levine, A.M., 2004, ApJ submitted, astro-ph/0407025
- Revnivtsev, M., Chernyakova, M., Capitanio, F., Westergaard, N. J., Shoenfelder, V., Gehrels, N., & Winkler, C., 2003, Atel 132
- Revnivtsev, M., Gilfanov, M., Sunyaev, R., Jahoda, K., & Markwardt, C., 2003, A&A, 411, 329
- Roques, J. P., Schanne, S., von Kienlin, A., et al., 2003, A&A, 411, L91
- Rupen, M. P., Mioduszewski, A. J., & Dhawan, V., 2003a, Atel 137
- Rupen, M. P., Mioduszewski, A. J., & Dhawan, V., 2003b, Atel 142
- Shakura, N. I. , & Sunyaev, R. A., 1973, A&A, 24, 337
- Shapiro, S. L., Lightman, A. P., & Eardley, D. M., 1976, ApJ, 204, 187
- Skinner, G., & Connell, P., 2004, A&A, 411, L123
- Sobczak, G. J., McClintock, J. E., Remillard, R. A., Cui, W., Levine, A. M., Morgan, E. H., Orosz, J. A., & Bailyn, C. D., 2000, ApJ, 544, 993
- Steeghs, D., Miller, J. M., Kaplan, D., & Rupen, M., 2003, Atel 146

- Sturner, S. J., Shrader, C. R., Weidenspointner, G., et al., 2003, *A&A*, 411, L81
- Sunyaev, R. A., & Titarchuk, L. G. , 1980, *A&A*, 86, 121
- Titarchuk, L. G., 1994, *ApJ*, 434, 570
- Vedrenne, G., Roques, J.-P., Schonfelder, V., et al., 2003, *A&A*, 411, L63
- Winkler, C., Courvoisier, T. J.-L., Di Cocco, G., et al., 2003, *A&A*, 411, L1
- Wood, K., Share, G., Johnson, N., Yentis, D., & Byram, E.T., 1978, *IAU Circ.*, 3203
- Zdziarski, A. A., Poutanen, J., Paciasas, W. S., Paciasas, W.S.,& Wen, L., 2002, *ApJ*, 578, 357
- Zdziarski, A. A., Gierlin'ski, M., Mikołajewska, J., Wardzin'ski, G., Smith, D.M., Alan Harmon, B., & Kitamoto, S., 2004, *MNRAS*, 351, 791

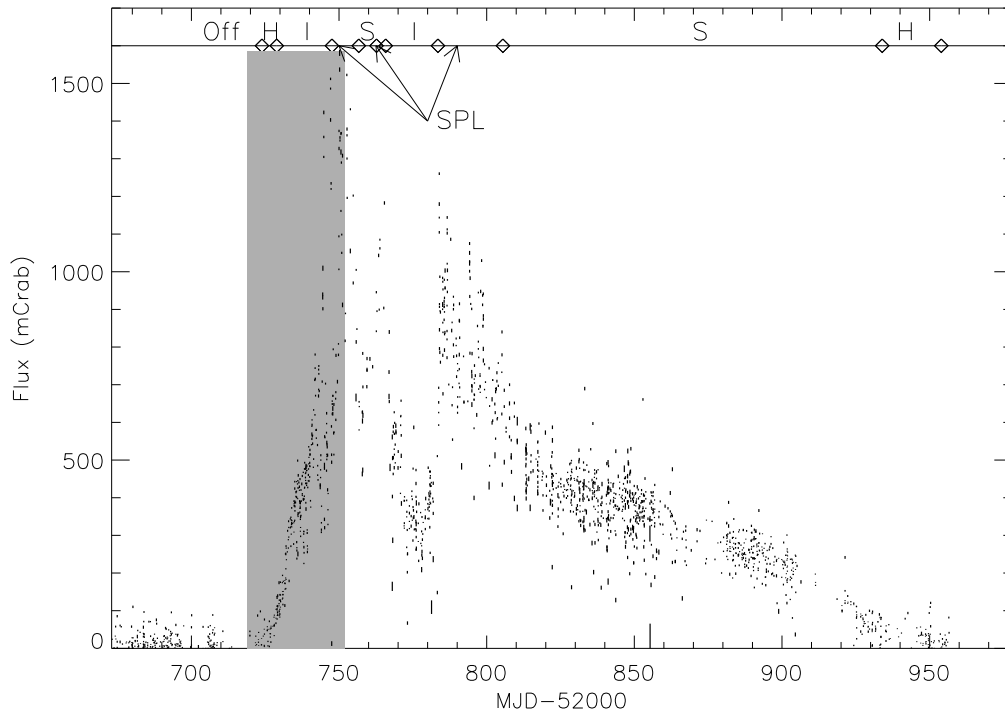


Fig. 1.— ASM/RXTE light curve (1.5-12 keV) covering the 2003 outburst of H1743-322. The different states summarized on the graph fulfill the criteria (see the text) of the spectral classification of McClintock & Remillard (2003). The corresponding legend is: Off : off, H: hard, I: intermediate, S: thermal dominant and SPL. The grey color bar shows the ASM/RXTE observations for which the SPI/INTEGRAL data have been analyzed. Figure 3 (see below) focuses on these observations.

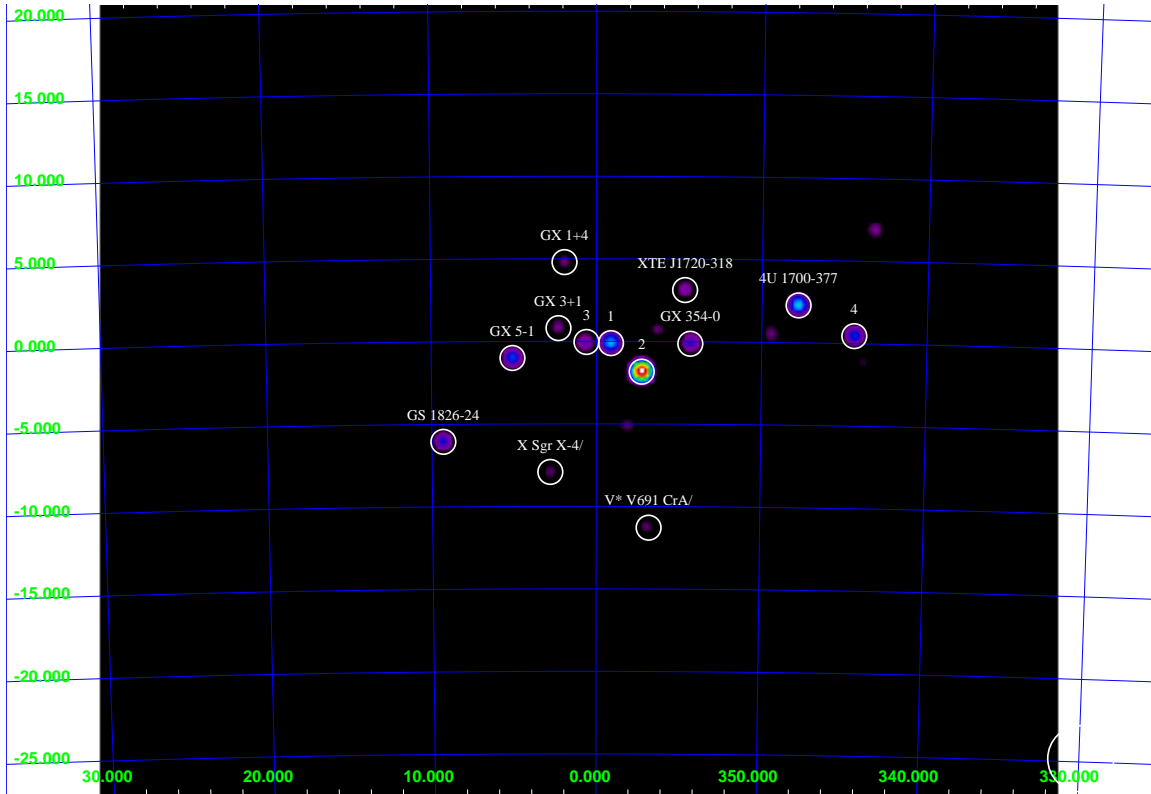


Fig. 2.— SPIROS image obtained using revolutions 56, 58, 59, 60, 61, 62 and 63 in the 20-36 keV energy range with a significance higher than  $5\sigma$ . The horizontal axis corresponds to the Galactic longitude and the vertical one to the Galactic latitude. The number corresponding to sources are 1 : 1E 1740.7-2942, 2 : H1743-322, 3 : IGR J17475-2822, 4 : OAO 1657-415.

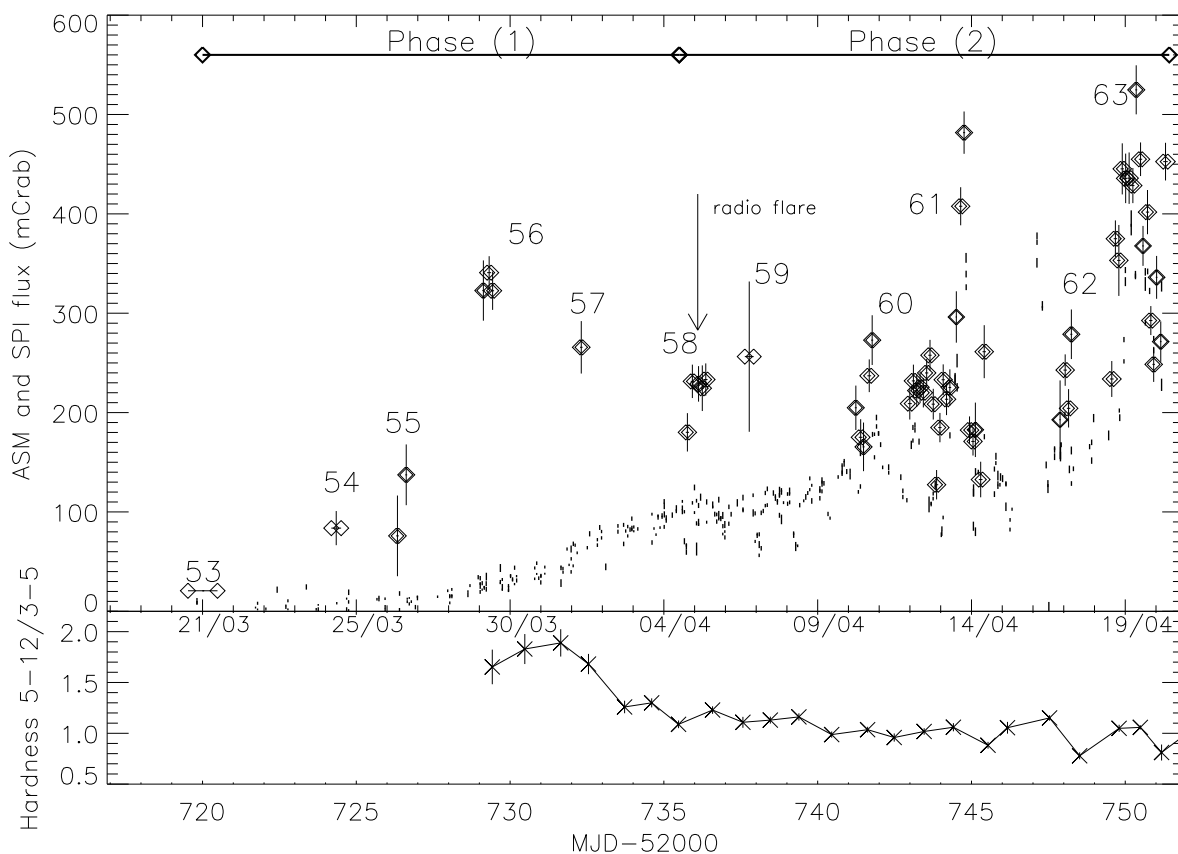


Fig. 3.— SPI light curve (diamonds) in the 20-36 keV energy range and ASM (thick bar) in the 1.5-12 keV energy range. The ASM flux has been divided by a factor of 4. We also give the revolution number and the period covered by each state of the source. An upper limit has been determined for revolution 53. The panel below the light curve shows the evolution of the hardness from the ASM/RXTE in the 3-12 keV energy range. A vertical arrow indicates the radio flare event (see section 1.).

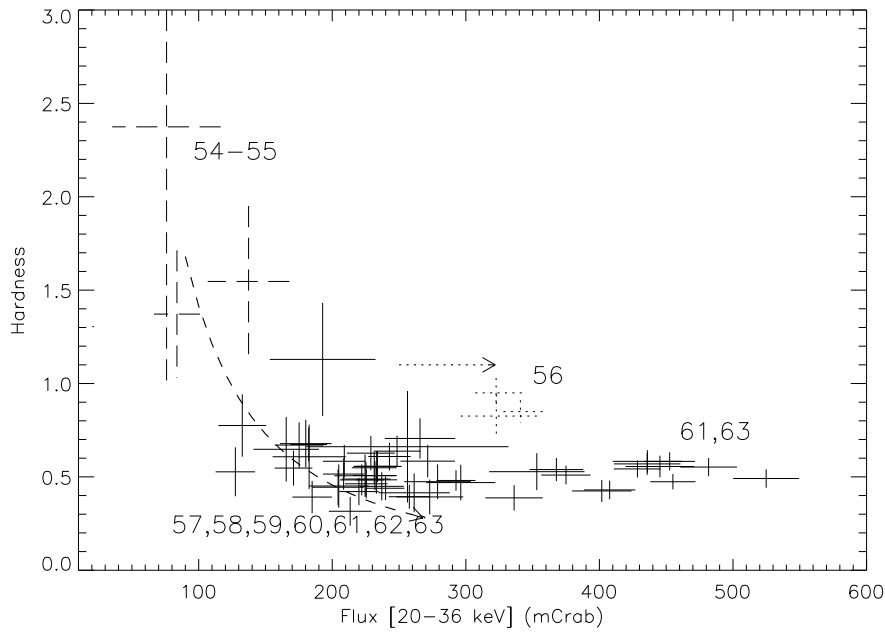


Fig. 4.— Overview of the hardness behaviour of H1743-322: in the hard state (revolutions 54-55 and 56, which are represented by dashed and dotted line respectively) and the intermediate/SPL state ( $\geq$  revolution 57). The horizontal and dotted arrow illustrates the increase of flux with a constant hardness from revolution 54-55 to revolution 56 (see section 5.3). A curved dashed line has been drawn to illustrate the negative hardness-flux correlation in the 20-36 keV energy range.

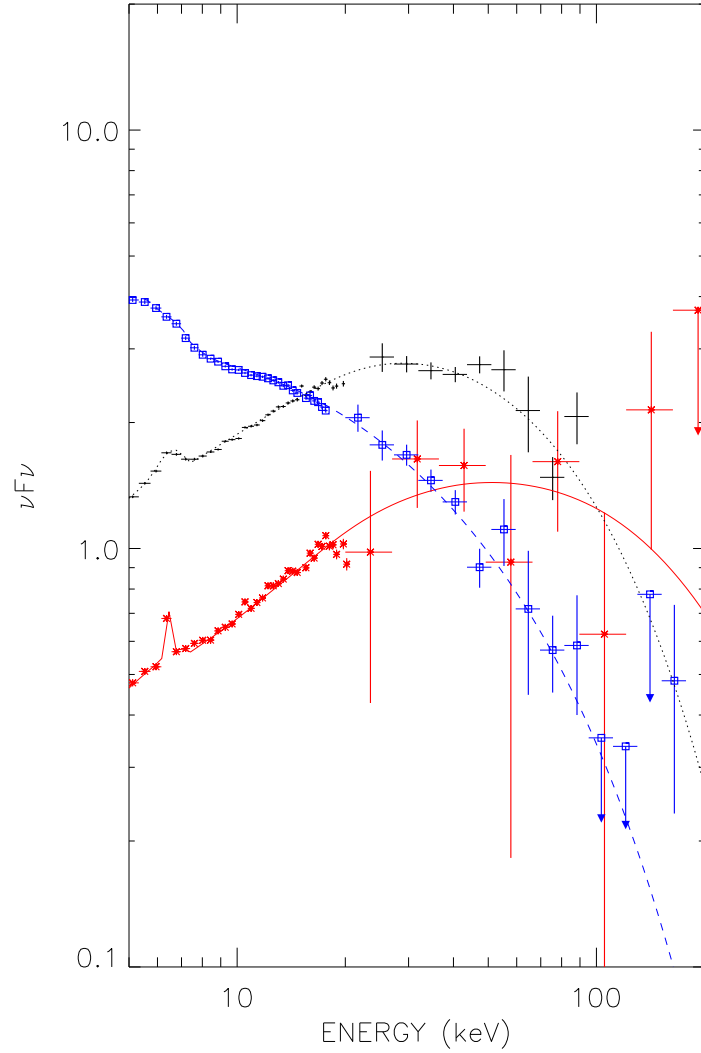


Fig. 5.— Spectra from simultaneous PCA/RXTE and SPI/INTEGRAL observations of H1743-322 during revolution 55 (red asterisks) and revolution 56 (green points) and during revolution 58 (blue squares). The model used is  $\text{FN} \times \text{smedge} \times \text{phabs} \times (\text{diskbb} + \text{pexrav} + \text{gaussian})$  (see Table 6).

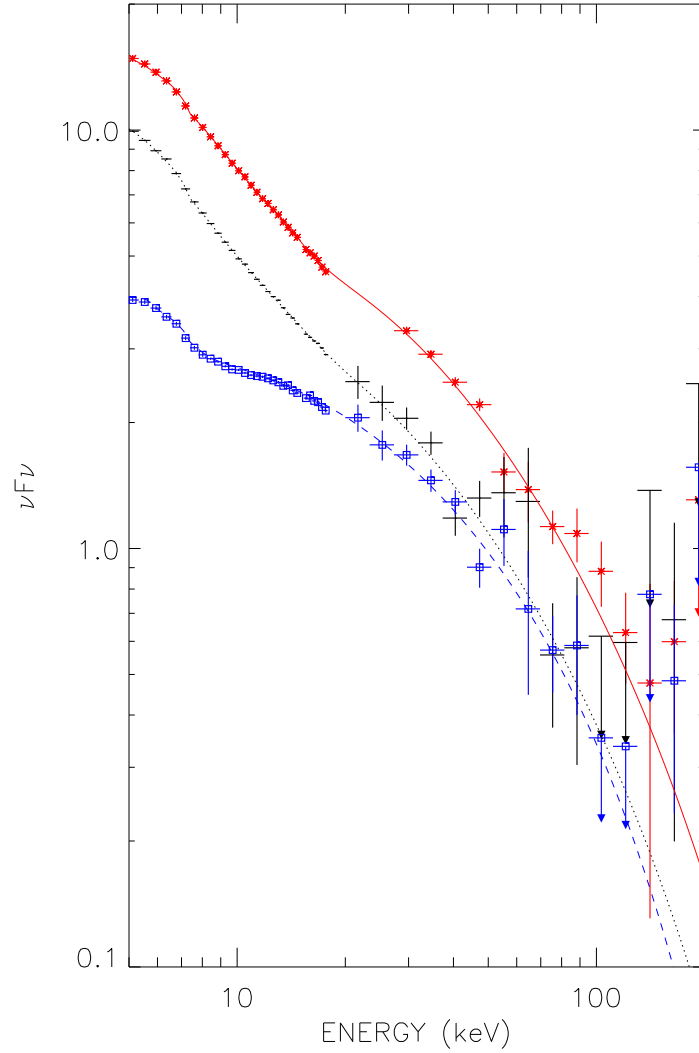


Fig. 6.— Spectra from simultaneous PCA/RXTE and SPI/INTEGRAL observations of H1743-322 during revolution 58 (blue square) , revolution 60-63 (no flare events) (red asterisk) and revolution 61-63 (flare events) (in green). The model used is  $\text{FN} \times \text{smedge} \times \text{phabs} \times (\text{diskbb} + \text{pexrav} + \text{gaussian})$  (see Table 6).

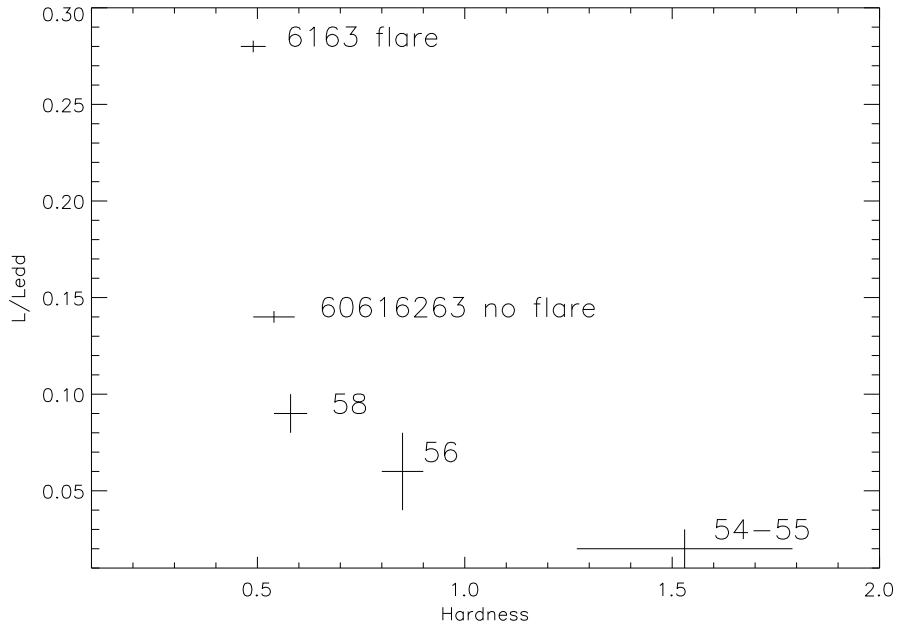


Fig. 7.— Evolution of the bolometric luminosity in Eddington luminosity  $L_{\text{Edd}}$  as a function of the hardness in the 23-200 keV energy range. A distance of 8.5 kpc has been assumed.

Rev.	st	SP <sub>start</sub>	SP <sub>stop</sub>	$\Delta t_{sp}$ (ks)	ID	RX <sub>start</sub>	RX <sub>stop</sub>	Exp.(ks)
53		52719.53	52720.49	23				
54		52723.77	52724.51	17.4				
55		52726.30	52726.65	7.6	80138	52726.80	52726.87	5.7
56		52729.10	52729.48	16.1	80138	52729.79	52729.83	3.6
57		52732.27	52732.35	4.0				
58*		52735.71	52736.42	61.2	80138	52735.71	52735.76	4.4
59		52737.63	52737.92	7.0				
60		52741.21	52741.80	23.2	80146	52741.83	52741.93	5.7
61	nf	52742.93	52744.6	71.9	80146	52743.22	52743.26	3.7
					80146	52743.22	52743.26	3.7
					80146	52744.20	52744.24	3.0
61	f	52744.60	52744.79	8.4				3.7
	nf	52744.79	52745.47	21.7	80146	52743.22	52743.26	3.7
62		52747.86	52748.28	17.9	80146	52747.61	52747.68	5.7
63	nf	52749.50	52749.62	7.0				
	f	52749.71	52750.78	40.1	80146	52750.27	52750.29	2.1
					80146	52750.31	52750.36	3.8
	nf	52750.78	52751.18	12.5	80146	52750.66	52750.97	27
					80146	52751.04	52751.08	3.7
					80146	52751.10	52751.14	3.1
	f	52751.23	52751.38	4.9	80146	52751.24	52751.34	8.3
					80146	52751.37	52751.40	2.1

\*: radio flare (Rupen et al. 2003b)

Table 1: The INTEGRAL observations of H1743-322 during AO-1: 2003-03-21 00:00:00 corresponds to IJD 1175 and MJD 52719. For each INTEGRAL revolution (Rev.), we give the beginning SP<sub>start</sub> and the end SP<sub>stop</sub> of the SPI observations in MJD.  $\Delta t_{sp}$  is the useful duration for SPI observations. The separation between flare (f) and non flare events (nf) for revolutions 61 and 63 has been specified in column "st". ID is the identification program number of RXTE observations. RX<sub>start</sub> and RX<sub>stop</sub> are the beginning and the end of RXTE observations taken simultaneously with SPI observations. Exp. is the exposure time for PCA/RXTE.

	Source name	Flux (mCrab)	Significance	Flux (mCrab)	Significance
		20-36 keV		90-120 keV	
1	H1743-322	$266.98 \pm 2.09$	127.2	$96.70 \pm 7.36$	13.1
2	1E <i>region</i> (a)	$108.31 \pm 2.35$	46.1	$79.00 \pm 7.14$	11.1
3	4U 1700-377	$158.47 \pm 3.30$	48.0	$55.03 \pm 8.83$	6.2
4	XTE J1720-318	$39.82 \pm 2.34$	17.0		
5	OAO 1657-415	$134.20 \pm 4.21$	31.9		
6	Ginga 1826-24	$73.23 \pm 2.65$	27.6		
7	IGR J17475-2822	$51.17 \pm 2.49$	20.5		
8	GX 5-1	$69.99 \pm 2.06$	33.9		
9	GX 354-0	$60.51 \pm 2.36$	25.6		
10	H 1702-429	$46.12 \pm 4.80$	9.6		
11	GX 1+4	$28.69 \pm 2.28$	12.6		
12	GX 3+1	$32.73 \pm 2.36$	13.9		
13	H 1820-303	$27.62 \pm 2.35$	11.7		
14	3A 1822-371	$30.15 \pm 2.50$	12.0		

note : 1 Crab = 0.19 counts /s in the 20-36 keV energy range

Table 2: Catalog of sources surrounding H1743-322 in the 20-36 keV and 90-120 keV energy range. (a) : due to the modest angular resolution, SPI cannot distinguish all the sources present around 1E 1740.7-2942.

Rev.	PCA/RXTE		SPI	
	$\Gamma_x$	$\chi^2(\text{dof})$	$\Gamma_\gamma$	$\chi^2(\text{dof})$
55	$1.40^{+0.03}_{-0.13}$	2.88(17)	$1.8^{+0.2}_{-0.2}$	0.9(10)
56	$1.33^{+0.17}_{-0.36}$	2.07(18)	$2.5^{+0.1}_{-0.1}$	2.7(14)
58	$2.36^{+0.06}_{-0.10}$	2.61(13)	$2.9^{+0.1}_{-0.1}$	0.9(15)
60 to 63 (nf)	$2.65^{+0.03}_{-0.04}$	1.59(18)	$3.1^{+0.1}_{-0.1}$	1.2(15)
61-63 (f)	$2.57^{+0.03}_{-0.03}$	1.34(17)	$3.0^{+0.1}_{-0.1}$	1.0(14)

(nf) refers to no flare events and (f) to flare events

Table 3: H1743-322 data from PCA and SPI fitted separately. SPI/INTEGRAL and PCA/RXTE data have been fitted using a powerlaw model and SMEDGE×PHABS×(DISKBB+POWERLAW+GAUSSIAN) (see section 5.4 concerning the parameters of each components) respectively. The iron line width was kept free (except for the rev 55,56 and 58: it was fixed at 1.0 keV).  $\Gamma_x$  and  $\Gamma_\gamma$  are the photon powerlaw indices in the 3-14 keV energy band and in the 20-100 keV energy band respectively.

Rev.	FN	$\Gamma_\gamma$	$\chi^2(\text{dof})$	FN	$\Gamma'_\gamma$	$E_{cut}(keV)$	$\chi^2(\text{dof})$
55	1.3	$1.43^{+0.01}_{-0.01}$	2.8(41)	0.8	$1.0^{+0.2}_{-0.2}$	$46^{+20}_{-11}$	2.2(40)
56	0.8	$1.57^{+0.01}_{-0.01}$	11.0(48)	0.7	$1.2^{+0.1}_{-0.1}$	$40^{+6}_{-3}$	1.6(47)
58	1.6	$2.47^{+0.01}_{-0.01}$	3.8(46)	1.2	$2.1^{+0.1}_{-0.1}$	$25^{+2}_{-3}$	1.4(45)
60 to 63 (nf)	0.9	$2.81^{+0.02}_{-0.02}$	2.7(45)	0.8	$2.5^{+0.1}_{-0.1}$	$70^{+56}_{-23}$	1.9(44)
61-63 (f)	0.7	$2.76^{+0.02}_{-0.02}$	3.2(43)	0.7	$2.6^{+0.1}_{-0.1}$	$103^{+25}_{-29}$	1.8(42)

(nf) refers to no flare events and (f) to flare events

Table 4: H1743-322 data from PCA and SPI fitted jointly using : FN×SMEDGE×PHABS×(DISKBB+POWERLAW+GAUSSIAN) (see section 5.4 concerning the parameters of each components). FN is the normalization factor between SPI/INTEGRAL and PCA/RXTE.  $\Gamma_\gamma$  is the photon powerlaw index. POWERLAW was replaced by a cutoff powerlaw model :  $\Gamma'_\gamma$  and  $E_{cut}$  are the photon powerlaw index and the energy cutoff respectively. The iron line width was kept free (except for the rev 55,56 and 58: it was fixed at 1.0 keV).

rev	$T_{in}$ keV	$\tau$	kT keV	$\Phi_\gamma \times 10^{-9}$ ERG	$\Phi_{bb} \times 10^{-9}$ ERG	$\Phi_{disc}$ %	$EW$ eV	FN	$\chi^2(\text{dof})$
55	$0.27^{+0.02}_{-0.03}$	$3.13^{+0.03}_{-0.03}$	$17^{+3}_{-5}$	0.08	0.2	2	74	0.9	1.99(37)
56	$0.41^{+0.02}_{-0.01}$	$3.39^{+0.03}_{-0.09}$	$15^{+1}_{-1}$	0.05	0.4	2	147	0.9	1.58(48)
58	$0.39^{+0.10}_{-0.02}$	$1.00^{+0.10}_{-0.11}$	$22^{+5}_{-5}$	1.58	5.9	7	245	1.5	0.74(50)
6061 nf	$0.62^{+0.04}_{-0.04}$	$0.25^{+0.03}_{-0.03}$	$38^{+2}_{-2}$	1.02	7.2	7	143	0.7	2.00(44)
6163 fl	$0.65^{+0.03}_{-0.01}$	$0.26^{+0.03}_{-0.02}$	$37^{+2}_{-2}$	4.89	6.7	32	173	0.5	2.57(41)

(nf) refers to no flare events and (f) to flare events, ERG = ergs cm<sup>-2</sup> s<sup>-1</sup>

Table 5: Simultaneous PCA-SPI fit with a Comptonization model. The model used was described by the following XSPEC components (explained in section 5.4): FN×SMEDGE×PHABS×(DISKBB+COMPTT+GAUSSIAN).  $T_{in}$  is the inner disk temperature,  $\tau$  the optical depth and kT the plasma temperature.  $\Phi_\gamma$  and  $\Phi_{bb}$  (with an error of 10 %) are the flux in the 20-100 keV energy range and the flux of the disk blackbody component in the 2-20 keV energy range respectively.  $\Phi_{disc}$  is the disc-flux fraction in the 2-20 keV energy range. The iron line width was kept free (except for the rev. 61,63 during the flaring activity : it was fixed at 0.1 keV) and  $EW$  is the equivalent width. FN is the normalization factor between SPI/INTEGRAL and PCA/RXTE.

Rev.	$T_{in}$ keV	$\Gamma$	$E_{cut}$ keV	$\Omega/2\pi$	FN	$\chi^2(\text{dof})$
55	$0.29^{+0.36}_{-0.29}$	$1.07^{+0.15}_{-0.19}$	$80^{+145}_{-37}$	0.5 fr	1.0	1.47(40)
56	$0.34^{+0.46}_{-0.08}$	$1.45^{+0.12}_{-0.18}$	$62^{+13}_{-21}$	$0.58^{+0.21}_{-0.32}$	1.0	1.30(46)
58	$0.37^{+0.31}_{-0.06}$	$2.37^{+0.06}_{-0.05}$	$71^{+26}_{-17}$	$0.43^{+0.25}_{-0.12}$	1.3	0.80(45)
6063 nf	$1.33^{+0.03}_{-0.03}$	$2.58^{+0.10}_{-0.15}$	$88^{+85}_{-37}$	$0.49^{+0.26}_{-0.29}$	0.8	1.70(42)
6163 f	$1.57^{+0.01}_{-0.01}$	$2.58^{+0.03}_{-0.03}$	$99^{+28}_{-19}$	0.5 fr.	0.8	2.39(39)

(nf) refers to no flare events and (f) to flare events

Table 6: Simultaneous PCA-SPI fit with the Reflection model. The model used was described by the following XSPEC components (explained in section 5.4): FN×SMEDGE×PHABS×(DISKBB+PEXRAV+GAUSSIAN).  $T_{in}$  is the inner disk temperature,  $\Gamma$  the powerlaw photon index and  $E_{cut}$  the energy cutoff.  $\Omega/2\pi$  is the reflection scaling factor. The iron line width was kept free (except for the rev. 61,63 during the flaring activity : it was fixed at 0.1 keV). FN is the normalization factor between SPI/INTEGRAL and PCA/RXTE.